MICROBOONE-NOTE-1048-PUB

Detector calibration using through going and stopping muons in the MicroBooNE LArTPC

The MicroBooNE Collaboration

microboone_info@fnal.gov

August 6, 2018

Abstract

The MicroBooNE experiment at Fermilab uses a liquid argon time projection chamber (LArTPC) in the Booster Neutrino Beam to search for anomalous production of electron-neutrino-like events and to study neutrino-argon cross sections in the 1 GeV neutrino energy regime. The detector operates at 0.273 kV/cm drift electric field and its TPC has an active mass of 85 tons of liquid argon. One of the main advantages of the LArTPC technology is its ability to reconstruct both particle track direction and energy with very high precision. Effects such as misconfigured or cross-connected TPC wires, space charge effects, electron attenuation, diffusion, and recombination can worsen the energy resolution of the detector. Therefore the detector calibration is of utmost importance to get the correct dE/dx (energy loss per unit track length) measurement. This is crucial for particle identification and in particular the separation of electrons and photons, essential for oscillation analyses. Here we describe a method developed for MicroBooNE to calibrate the detector by correcting for the above mentioned effects. In this analysis first we make the detector response uniform throughout the detector and time using through-going muons. Next stopping muons are used to determine the energy scale and convert dQ/dx to dE/dx.

Contents

1 Introduction **3**

2 Calibrating the MicroBooNE detector **3**
2.1 dQ/dx calibration . . . 3
2.1.1 Misconfigured or cross-connected TPC channels . . . 4
2.1.2 Space charge effects (SCE) . . . 4
2.1.3 Electron attenuation . . . 5
2.1.4 Diffusion . . . 5
2.1.5 Recombination . . . 6
2.1.6 Temporal variations . . . 6
2.1.7 dQ/dx variation . . . 6
2.2 dE/dx calibration . . . 7

3 Event selection **8**
3.1 Selection cuts (dQ/dx calibration) . . . 8
3.2 Selection cuts (dE/dx calibration) . . . 9

4 Data sample **10**

5 Analysis method **10**
5.1 Detector calibration in YZ plane . . . 10
5.2 Drift direction calibration of the detector . . . 11
5.3 Time dependent calibration of the detector . . . 12
5.4 dE/dx calibration of the detector . . . 14

6 Results **16**
6.1 dQ/dx calibration . . . 16
6.1.1 dQ/dx calibration (Monte Carlo) . . . 16
6.1.2 dQ/dx calibration (data) . . . 16
6.2 dE/dx calibration . . . 17
6.2.1 Validation of calorimetric energy reconstruction . . . 18

7 Angular dependence study **20**

8 Conclusions **20**

Appendix A **24**

1 Introduction

The liquid argon time projection chamber (LArTPC) technology provides both particle track and energy reconstruction capabilities with very high resolution. Because of this feature, LArTPC detectors are also categorized as imaging detectors and have shown great potential already. The basic working principle of a LArTPC neutrino detector is that neutrinos first interact with an argon nucleus and produce both secondary particles (charged and neutral) and light copiously. The produced scintillation light is collected by photon detectors inside the cryostat. The secondary charged particles travel through liquid argon and mainly loose their energy by ionizing argon atoms. The ionization electrons travel to the anode wire planes under an applied electric field. One can use light detected by the photon detectors along with charge measured using the anode wire planes in order to reconstruct particle trajectories and energies. The first step of energy reconstruction in LArTPC detectors involves the extraction of charge information from the signals (waveforms) of the anode plane wires. The MicroBooNE experiment[1] uses several signal processing techniques [2, 3] including noise filtering and deconvolution for charge extraction. However, the total charge extracted in this way normally does not reconstruct the total charge released from ionization due to a number of reasons. Among those reasons, distortions in detector response due to misconfigured or cross-connected TPC channels [4], space charge effects (SCE) [5, 6], electron attenuation [7, 8, 9, 10, 11, 12, 13], diffusion and recombination are the most significant. So to trace back the exact amount of charge released from the original interaction, one has to correct for all of these effects starting from the dQ/dx[1] values. Correcting the TPC signal for these effects is known as the dQ/dx calibration (relative calibration) of the detector. Once we have reliable charge information, we can calculate the exact amount of energy loss due to ionization and this process of determining energy is known as the dE/dx calibration (absolute calibration) of the detector. More details about dQ/dx and dE/dx calibration of the detector will be discussed in coming sections.

2 Calibrating the MicroBooNE detector

The detector calibration applied, consists of two steps. In the first step we make the detector response to ionization charge uniform throughout the detector and in time. This process is known as the dQ/dx calibration of the detector. Once the detector response is uniform throughout the TPC and in time, calibration constant is determined to convert ionization charge per unit length dQ/dx to particle energy loss per unit length dE/dx. This process is known as the dE/dx calibration of the detector. In this analysis we focus on calibrating only the collection wire plane (plane 2) of the detector for both Monte Carlo and data. The calibration of induction planes is generally more difficult in particular because of the large angular dependence of the detector response. New techniques are being developed to improve the reconstruction of the induction plane signals [2, 3], which will allow reliable dE/dx measurement on induction plane wires in the future. In addition, the forthcoming space charge effect calibration will address the residual angle dependence of dE/dx values on top of the improvements introduced by signal processing. The two-step calibration procedure is motivated by the similar calibration techniques developed for other calorimeters such as the MINOS detectors [14].

2.1 dQ/dx calibration

In the dQ/dx calibration step, we separate the detector non-uniformities into three categories and calibrate them in sequence:

- detector non-uniformities in the YZ plane,
- detector non-uniformities in the drift (X) direction, and

[1]Here and later in dE/dx the notation dx refers to the length of the particle track seen by a wire on a wire plane, which should not be confused with an infinitesimal distance in X (drift) direction of the TPC.

- variation of detector response over time.

Non-uniformities in the detector response in the YZ plane are primarily caused by misconfigured or cross-connected TPC channels, space charge effects, and transverse diffusion, while the non-uniformities in the drift direction are mainly caused by electron attenuation, space charge effects (through both distortions of tracks and changes to the electric field), and longitudinal diffusion. It should be noted that the calibration scheme described here is an approximation because effects such as space charge cannot be completely factorized in separate YZ plane and drift direction effects: for a given X value, the variations in the YZ plane are different. Ideally we should carry out this calibration by voxelizing the detector into small XYZ cubes and derive a calibration constant for each cube. But limited statistics makes this approach impractical. Moreover spatial distortions introduced by space charge effects on track reconstruction are not addressed by this calibration scheme.

2.1.1 Misconfigured or cross-connected TPC channels

There are several identified issues with the MicroBooNE electronics and wire planes that can affect the TPC response to the ionization signals. These effects include ASIC misconfiguration, which can change the gain of certain electronic channels, and cross-connected or touching wires, which can distort the electric field between wire planes. They affect roughly 10% of the channels. As a consequence, the TPC response has a dependence on the location of charge deposition in the TPC, which needs to be calibrated out.

2.1.2 Space charge effects (SCE)

Since MicroBooNE is a surface-based detector, we see many cosmic-ray induced tracks inside the detector. Because of this, there is a significant accumulation of slow-moving positive argon ions inside the detector, which is enough to distort the uniformity of the drift electric field. These distortions in the electric field inside the TPC have two significant effects:

- distortions in the magnitude of the drift electric field, and
- distortions in the direction of the drift electric field.

When the magnitude of the electric field is distorted, the recombination of electrons and ions is affected. This recombination effect [15] is very sensitive to the changes in the electric field. When the drift electric field is relatively low, recombination becomes dominant, while at higher fields the effect is suppressed. Moreover, space charge effects can lead to spatial distortions in the trajectories of reconstructed particle tracks and electromagnetic showers. The positive argon ions collected tend to drag ionization electrons closer to the middle of the detector: tracks that are reconstructed closer to the cathode suffer offsets in their start and end points closer to the detector edge. The space charge effects are expected to be stronger at the detector edges transverse to the drift direction. The cumulative effect of the space charge in track reconstruction leads to squeezing of the reconstructed track in transverse directions and bending towards the anode.

Figure 1 shows how the SCE changes dQ/dx values over the entire drift distance of MicroBooNE [12]. As seen in the right plot of the figure, the dQ/dx values closer to the cathode are much higher compared to that of the anode. The accumulation of positive ions causes the electric field closer to the cathode to be approximately 10% higher than at the anode. The higher field suppresses electron-ion recombination near the cathode. In addition, due to spatial distortions, tracks reconstructed closer to the cathode are bent and squeezed making reconstructed dx values smaller. Thus we observe a higher collected charge per unit of reconstructed length closer to the cathode.

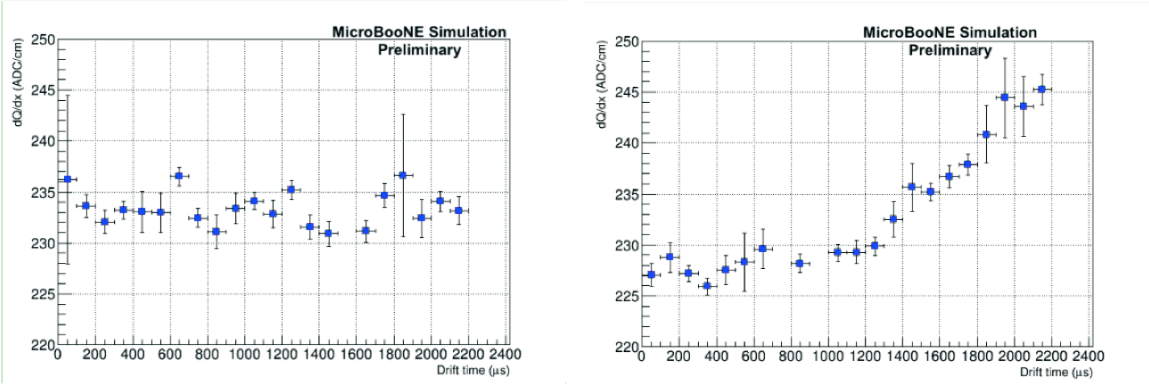

Figure 1: Plots of dQ/dx vs drift difference generated using Monte Carlo samples of isotropic single muons. In both of the samples diffusion is completely turned off and the electron lifetime is set very high. The plots show how dQ/dx changes over drift distance when a cloud of ionization electrons drifts from the cathode to the anode with and without space charge effects. In the left plot, space charge effects are turned off; in the right plot, space charge effects are turned on. Both plots are created using collection plane information.

2.1.3 Electron attenuation

When a cloud of ionization electrons drifts from the cathode to the anode, electronegative contaminants such as H_2O and O_2 can capture some of the drifting electrons reducing the final dQ/dx measured at the wire planes.

Equation 1 governs how a cloud of ionization electrons gets depleted due to capture by electronegative contaminants as the electrons drift towards the anode:

$$\frac{n_e(t_{\text{drift}})}{n_e(t_0)} = \exp\left(\frac{-(t_{\text{drift}} - t_0)}{\tau}\right), \tag{1}$$

where

$n_e(t_0)$ – Initial number of electrons,

$n_e(t_{\text{drift}})$ – Number of electrons after a time t_{drift} - t_0, and

τ – Electron lifetime.

The electron lifetime depends on the amount of electronegative contaminants present in the medium, where higher electron lifetime signals low contamination levels. Figure 2 shows the effect of electron attenuation on final dQ/dx values.

2.1.4 Diffusion

The diffusion can be studied under two categories:

- longitudinal diffusion, and
- transverse diffusion.

The cloud of ionization electrons tends to get smeared out in the direction of the drift because of the longitudinal diffusion. This could make the signal produced at longer drift distance wider and bias

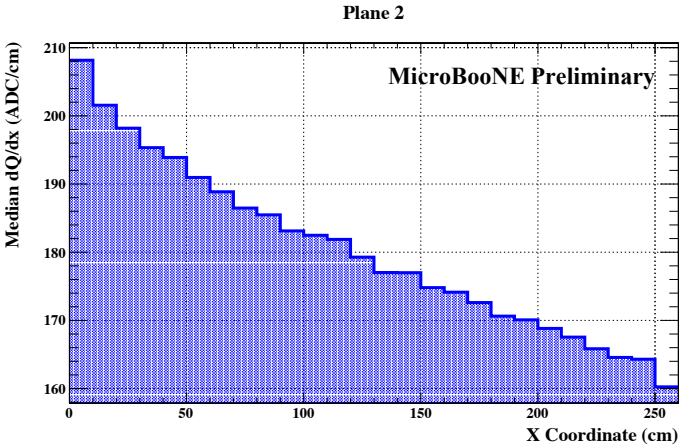

Figure 2: Change of dQ/dx as a function of drift distance in low argon purity data run 5691. Here median dQ/dx value is plotted for 10 cm wide bins in drift direction in the collection plane. The dQ/dx value drops from the anode to the cathode. This is due the fact that electronegative contaminants capturing ionization electrons.

the reconstructed charge. On the other hand, due to transverse diffusion some of the charge can leak into the neighboring wires from the target wire. These diffusive processes can introduce a bias in reconstructing dQ/dx values.

2.1.5 Recombination

When a charged particle traverses the liquid argon it produces both positive argon ions and ionization electrons. Some ionization electrons cannot completely liberate from their parent argon ions and recombine with parent ions to form neutral argon atoms again. This process is known as electron-ion recombination; a result of this effect is an underestimation of particle energy loss due to ionization if no correction is made. As already mentioned in the section 2.1.2, recombination is highly sensitive to the changes in the drift electric field.

2.1.6 Temporal variations

The detector response can change over time because of effects such as drift of the electronics gains, changes of temperature, different running conditions, etc. Note the time referred to here is the calendar time, not to be confused with drift time in the TPC. The most significant time-dependent change affecting MicroBooNE calibrations are changes in purity.

2.1.7 dQ/dx variation

Figure 3 shows the variation of detector response (dQ/dx) in YZ plane and in the drift direction X inside the TPC under the influence of various convoluted detector effects.

In the dQ/dx calibration of the detector, we aim to remove the aforementioned detector effects from the detector response. In other words, the dQ/dx calibration involves making the dQ/dx values uniform through out the detector and also in time. In this calibration process we use minimum ionizing cosmic muons as the standard candle for uniform energy deposition throughout the detector. These cosmic muons have typical momenta in the range of 4 GeV - 5 GeV, and deposit $\sim$ 1.7 MeV/cm. The dQ/dx calibration of the detector response is carried out in three separate steps:

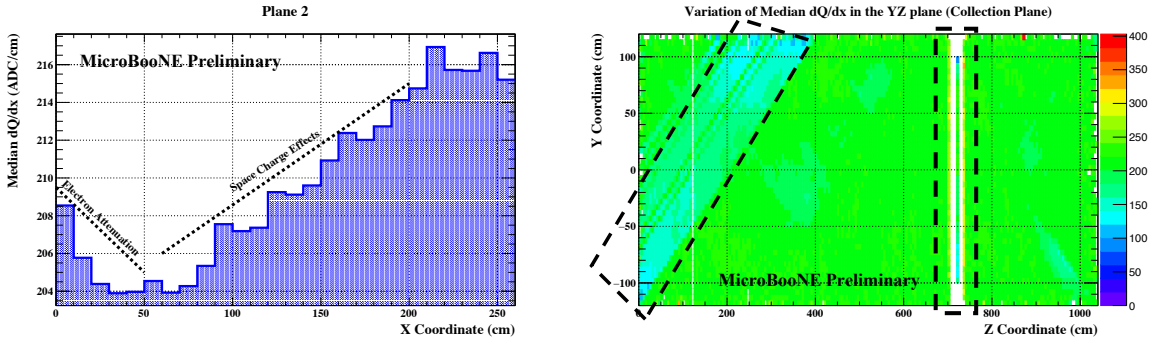

Figure 3: Variation of dQ/dx in the drift direction (left) and in the YZ plane (right) in data due to various convoluted detector effects in the collection plane. In the right plot the region inside the highlighted boundaries shows the effect of misconfigured or cross-connected TPC channels. The colors in the right plot represent the median dQ/dx value for a given 5 cm $\times$ 5 cm cell in the YZ plane. Both plots are created using the collection plane information.

- calibration of the detector in the YZ plane,
- calibration of the detector in the drift direction, and
- calibration of the detector in time.

Exact method used for dQ/dx calibration will be discussed in Section 5 in detail.

2.2 dE/dx calibration

Once the detector response becomes uniform after the dQ/dx calibration, the absolute energy scale can be determined. To move from the calibrated dQ/dx to dE/dx, we use the modified box model [15] for recombination as described in Equation 2.

$$\left(\frac{dE}{dx}\right)_{calibrated} = \frac{\exp\left(\frac{(\frac{dQ}{dx})_{\text{calibrated}}}{C}\frac{\beta' W_{\text{ion}}}{\rho \mathscr{E}}\right) - \alpha}{\frac{\beta'}{\rho \mathscr{E}}}, \tag{2}$$

with

C – Calibration constant to convert ADC values to number of electrons

W_{ion} – 23.6 x 10^{-6} MeV/electron (work function of argon)

$\mathscr{E}$ – 0.273 kV/cm (MicroBooNE drift electric field)

ρ – 1.38 g/cm^3 (liquid argon density at a pressure 18.0 psia)

β' – 0.212 (kV/cm)(g/cm^2)/MeV

α – 0.93

The last two parameters were measured by the ArgoNeuT experiment [15] at an operational electric field of 0.481 kV/cm.

According to the above equation, precise determination of the calibration constant C which translates the "ADC/cm" to "number of electrons/cm", is important in determining the absolute energy scale. Here the goal of dE/dx calibration is to provide the calibration constant C.

In this particular calibration scheme, we are using stopping muons as the standard candle, because they have a well-understood energy loss profile. The stopping muons could either be isolated from cosmic data or neutrino interactions. The exact method we are using for dE/dx calibration will be discussed in Section 5 in detail.

3 Event selection

As described in Section 2, through-going cosmic muons are used for the dQ/dx calibration and stopping muons from neutrino interactions are used for the dE/dx calibration. Each muon in the selection is "tagged" with an initial time t_0, with respect to which drift time is measured.

3.1 Selection cuts (dQ/dx calibration)

For the dQ/dx calibration of the detector we chose to use the anode-cathode crossing muons. The main reason is that the anode-cathode crossing muons span over the whole drift distance, which make them the perfect sample to study any effects that depend on the drift distance. The crossing muons have a wide spatial but limited angular coverage. Figure 4 shows the presence of cosmic muons in our data.

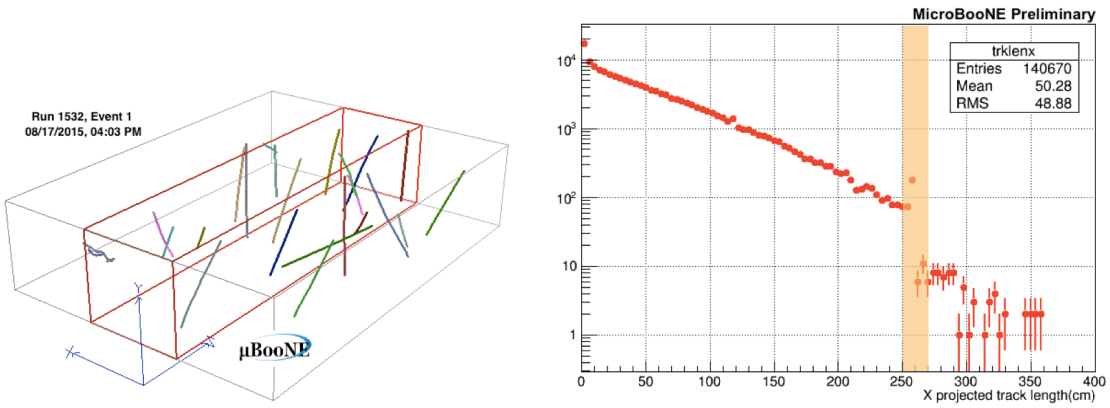

Figure 4: (Left) Presence of cosmic muons in MicroBooNE's 4.8 ms wide read out window. The colored tracks are the cosmics. (Right) The color band shows the presence of anode-cathode crossing tracks in cosmic data. It has been estimated in a $\sim$ 5000 event cosmic data sample $\sim$ 2% of the tracks are anode-cathode crossing tracks. The 20 cm window is selected to account for mis-reconstructions in track start and end points.

The tracks used in the dQ/dx calibration should satisfy the following selection criteria.

- 250 cm $<$ Track projected X length $<$ 270 cm : Any track that satisfies this selection cut is considered to be an anode-cathode crossing track. A 20 cm wide window is selected in order to account for imperfect reconstruction of track start and end positions.
- Absolute value of track angle θ_{XZ} (see Figure 5) should not be in the region of 75° to 105° : This selection cut ensures that we are excluding the tracks which are going into the wire planes (these tracks tend to be mis-reconstructed).
- Absolute value of track angle θ_{YZ} (see Figure 5) should not be in the region of 80° to 100° : This selection cut helps to remove tracks that are nearly parallel to the collection plane wires. See Figure 6. The difference between Monte Carlo and data in these figures is due to the fact that Monte Carlo is not simulating the effects such as SCE, field response, etc perfectly.

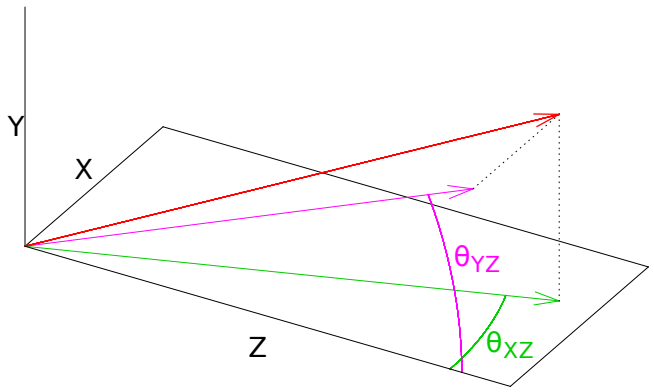

Figure 5: Definition of angle θ_{XZ} and θ_{YZ}.

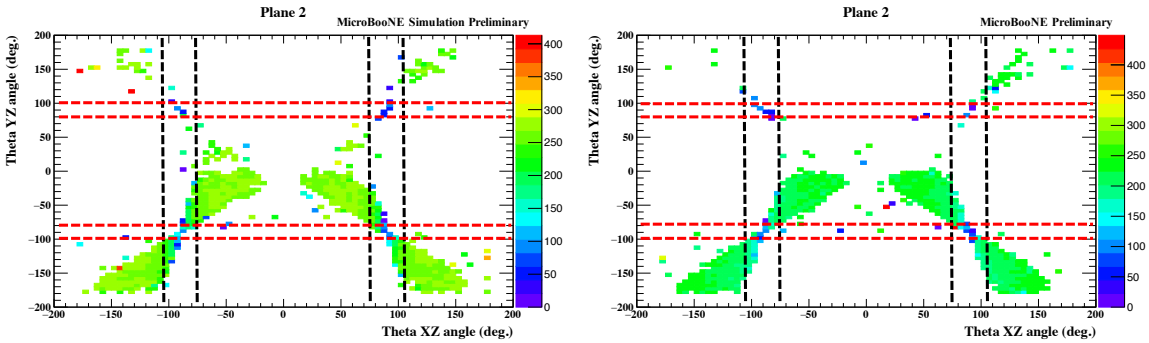

Figure 6: Variation of average dQ/dx values in the phase space of θ_{XZ} and θ_{YZ} in the collection plane. The Z axis represents average dQ/dx for a track which has a given θ_{XZ} and θ_{YZ} angular orientation. The units of the Z axis is in MeV/cm. The regions inside dashed lines show the angles excluded for crossing tracks discussed in Section 3.1 for the collection plane. Left: Monte Carlo; Right: Data.

3.2 Selection cuts (dE/dx calibration)

In the dE/dx calibration of the detector, we employ stopping muons induced by the neutrino interactions. We use the following set of selection cuts to isolate these muons from Monte Carlo:

- 10 cm < reconstructed start(end) point X < 250 cm, -110 cm < reconstructed start(end) point Y < 110 cm and 10 cm < reconstructed start(end) point Z < 1030 cm : These selection cuts ensure that possible reconstructed muons are well contained within the TPC.
- Reconstructed track should match to a stopping muon which comes from a neutrino interaction using truth information (this applies only to Monte Carlo).
- The distance between start(end) point of the true track and start(end) point of the reconstructed track < 5 cm : This cut further makes sure that we are getting the correct reconstructed muon track (this applies only to Monte Carlo).
- Absolute value of reconstructed track angle θ_{XZ} should not be in the region of 75° to 105° : This selection cut ensures that we are excluding the tracks which are going into the wire planes.

- Absolute value of reconstructed track angle θ_{YZ} should not be in the region of 80° to 100°: This selection cut ensures that we are excluding the tracks which are nearly parallel to the collection plane wires.

To isolate the stopping muons in data, the following selection criteria are applied:

- Run the CC Selection II Filter [27] to isolate primary muons from charge current interaction.
- Use the same track containment and angular cuts as applied to the Monte Carlo sample.
- Calculate the median dQ/dx values of the track in the first and last 5 cm segments. If the ratio of the two median dQ/dx values in the last 5 cm segment and the first 5 cm segment is greater than 1.5, the track is selected as a stopping muon. This cut aims to find the Bragg peak and remove poorly reconstructed tracks. The cut value is determined from the Monte Carlo sample where well reconstructed stopping muons are selected.

4 Data sample

The dQ/dx calibration of the detector is carried out using both data and Monte Carlo. For Monte Carlo we use Corsika cosmic simulations [28] overlaid with neutrino interactions to get the anode-cathode crossing cosmic muons while for data we use the entire Run I data to get crossing muons. The time period of data used ranges from February to October of 2016. In both Monte Carlo and data we use the **pandoraCosmicKalmanTrack** [29] tracking algorithm to reconstruct particle tracks, which performs pattern recognition and a Kalman filter fit to the cosmic ray muon tracks.

The dE/dx calibration of the detector is also done for both Monte Carlo and data. For Monte Carlo we use a cosmic overlaid neutrino sample to get stopping muons induced by the neutrino interactions, where these stopping muons are reconstructed using the the track algorithm **pandoraNu** [29], which is optimized to reconstruct particles produced by the neutrino interactions with argon. In data we apply the CC Selection Filter II over 5E19 run I unblinded dataset to get candidate muons from charged current interactions. A similar study was done using stopping cosmic ray muons [30].

5 Analysis method

The dQ/dx calibration of the detector is carried out in 3 separate steps for the collection plane.

- Step 1 : Detector calibration in YZ plane - This step aims to remove the effects from space charge effects, misconfigured or cross-connected anode plane channels and transverse diffusion.
- Step 2 : Detector calibration in drift direction - This step aims to remove effects coming from electron attenuation, space charge effects and longitudinal diffusion.
- Step 3 : Detector calibration in time - This step aims to remove any temporal variations in the detector response. This step is done only for data not for Monte Carlo since there is no time dependence in Monte Carlo simulation.

5.1 Detector calibration in YZ plane

Once we have a data sample consisting of anode-cathode crossing tracks, we use the following procedure to get the detector calibration factors in the YZ plane.

- Crossing tracks are isolated : The selection of crossing tracks is described in the section 3.2.
- Filter out only the crossing tracks which pass the angular cuts described in the section 3.2.

- Starting time (t_0) of the track is calculated : For crossing muons the minimum drift coordinate is supposed to correspond to t_0.
- Once t_0 is known, the drift coordinate of each 3D point of that track is corrected by the knowledge of t_0.
- The YZ plane is segmented into 5 cm by 5 cm cells.
- Each 3D point on a track is grouped into its relevant cell in YZ plane by looking into their Y and Z coordinates : Here we select only the points which satisfy the conditions 0 cm $< X_{Corrected}$ $<$ 260 cm, -120 cm $<$ Y $<$ 120 cm and 0 cm $<$ Z $<$ 1040 cm.
- Once looping over all the crossing tracks, we select only the cells which have a population of more than 5 3D points.
- For each of the selected cells, we calculate the median dQ/dx value by considering charge information of all the 3D points in that cell. The median dQ/dx of a given cell is called the "Local Median dQ/dx" of that cell.
- Once the local median dQ/dx values are calculated for all the cells in YZ plane, the "Global Median dQ/dx" is calculated by taking the median dQ/dx value from all the 3D points coming from all crossing tracks.
- For each cell in YZ plane a correction factor $Corr(y, z)$ is defined using the Equation 3.

In data we derive correction factors in YZ plane only for 3 separate time periods. Time period I is from 2016 February to 2016 May, time period II is from 2016 June to 2016 July and time period III is from August 2016 to October 2016. The reason we combine data for different times, is due to the fact that, the dominant contributor for YZ plane irregularities is from effects introduced by misconfigured or cross-connected TPC channels and these effects do not vary with time significantly. For Monte Carlo we derived only a single set of YZ corrections for the collection plane.

$$Corr(y, z) = \frac{(dQ/dx)_{Global}}{(dQ/dx)_{Local}} \tag{3}$$

$(dQ/dx)_{Global}$ – Global median dQ/dx in the collection plane

$(dQ/dx)_{Local}$ – Local median dQ/dx for a given YZ plane cell in the collection plane

5.2 Drift direction calibration of the detector

Once the calibration in YZ plane is done, we move to the drift direction calibration of the detector. The following set of points explain how this calibration procedure is carried out.

- Crossing tracks are isolated which satisfy angular cut as explained in the procedure for YZ calibration.
- t_0 of the track is extracted and drift coordinates of all the 3D points of the track are corrected by this t_0.
- The charge information (dQ/dx) of each 3D point is corrected using YZ correction factors, derived in the previous step to remove the irregularities in YZ plane using the Equation 4. Here we select the 3D points which satisfy the conditions 0 cm $< X_{Corrected} <$ 260 cm, -120 cm $<$ Y $<$ 120 cm and 0 cm $<$ Z $<$ 1040 cm. Moreover we look into the Y and Z coordinates of the 3D point to decide as which YZ correction factor to use.

- The drift direction is segmented into 10 cm wide line segments in data and 5 cm wide line segments in Monte Carlo. The bin sizes are determined both in Monte Carlo and data so as to minimize the statistical fluctuations in correction factors.
- Each 3D point of the tracks is grouped into the relevant drift direction line segment based on its corrected X coordinate.
- For each of the line segments in drift direction which has more than five 3D points, we define a local "Median dQ/dx" as in the YZ calibration procedure.
- A "Global Median dQ/dx" is also defined as explained in the previous calibration procedure.
- Finally for each line segment in the drift direction, a correction factor $Corr(x)$ is defined using the Equation 5.

In data we derive drift direction correction factors daily as space charge effects and electron lifetime change significantly over time. To get a reliable set of correction factors, we need to have a data sample which is rich in statistics. For this purpose, we derive correction factors in drift direction only for the days where there are more than 40 crossing tracks that leave hits in the collection plane after all the angular cuts. For Monte Carlo we derive only a single set of drift direction correction factors for the collection plane as there is no time variation of space charge effects and electron attenuation.

$$(dQ/dx)_{YZ\_Corrected} = Corr(y,z) \cdot (dQ/dx)_{Reconstructed} \tag{4}$$

$(dQ/dx)_{YZ\_Corrected}$ – Corrected (dQ/dx) value by $Corr(y,z)$ correction factor for irregularities in the YZ plane

$(dQ/dx)_{Reconstructed}$ – Uncorrected dQ/dx value

$$Corr(x) = \frac{(dQ/dx)'_{Global}}{(dQ/dx)'_{Local}} \tag{5}$$

$(dQ/dx)'_{Global}$ – Global median dQ/dx value after correcting for YZ plane irregularities by Equation 4 in the collection plane

$(dQ/dx)'_{Local}$ – Local dQ/dx median for the given X segment after correcting for YZ plane irregularities by Equation 4 in the collection plane

5.3 Time dependent calibration of the detector

After step 1 and 2 we focus on the third step, which aims to remove any temporal variations in the detector response. The following set of steps explain how the detector calibration in time is achieved.

- Crossing tracks which satisfy the angular cuts are selected.
- All the 3D points are corrected by t_0 for their drift coordinate.
- The dQ/dx value of each 3D point is corrected using correction factors derived for YZ plane and drift direction using Equation 6 : Only the 3D points which satisfy the conditions 0 cm $< X_{Corrected} <$ 260 cm, -120 cm $<$ Y $<$ 120 cm and 0 cm $<$ Z $<$ 1040 cm are selected. Moreover the relevant correction factor in YZ plane and drift direction for a given 3D point is selected looking into its X,Y & Z coordinates.

- In the final step a "Global Median dQ/dx" value is defined in a way similar to step one and two. In the time calibration of the detector, we calculate this Global Median dQ/dx value on a daily basis.
- The global median dQ/dx values are plotted against time to visualize the detector variations in time.
- By visually scanning the plots in the Figure 7, a reference value (210 ADC/cm) for the global median dQ/dx in the collection plane is chosen.
- A time dependent correction $Corr(t)$ is determined using the Equation 7 for each day : The corrections are derived for three planes separately.

$$(dQ/dx)_{XYZ\_Corrected} = Corr(y,z) \cdot Corr(x) \cdot (dQ/dx)_{Reconstructed} \tag{6}$$

$(dQ/dx)_{XYZ\_Corrected}$ – Corrected dQ/dx value for YZ plane and drift direction irregularities in the collection plane

$(dQ/dx)_{Reconstructed}$ – Uncorrected dQ/dx value in the collection plane

$$Corr(t) = \frac{(dQ/dx)_{Reference}}{(dQ/dx)_{Global}} \tag{7}$$

$(dQ/dx)_{Reference}$ – Reference dQ/dx value in the collection plane

$(dQ/dx)_{Global}$ – Global dQ/dx value in the anode wire plane after correcting for YZ plane and drift direction irregularities

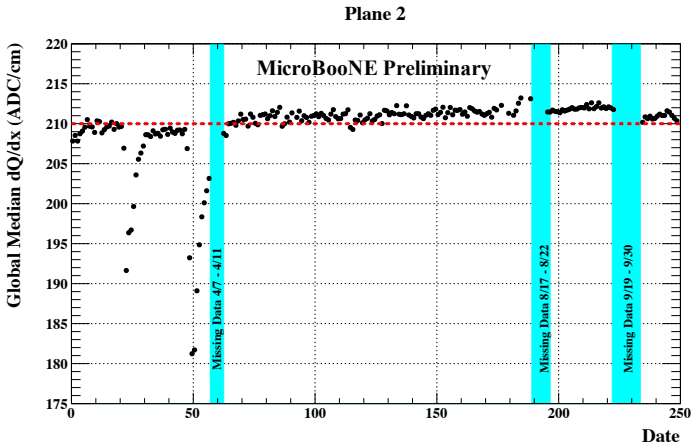

Figure 7: The variations of the Global Median dQ/dx over time in the collection plane. The red lines drawn shows the reference value selected which is 210 ADC/cm.

Once we are done with calibrating the detector in YZ plane, drift direction and in time, we can use the Equation 8 and Equation 9 to get the calibrated dQ/dx values in data and Monte Carlo respectively.

$$(dQ/dx)^{data}_{XYZT\_Corrected} = (dQ/dx)_{Reconstructed} \cdot Corr(y,z) \cdot Corr(x) \cdot Corr(t) \tag{8}$$

$(dQ/dx)^{data}_{XYZT\_Corrected}$ – Corrected dQ/dx for YZ plane, drift direction irregularities and time variations in data in the collection plane

$(dQ/dx)_{Reconstructed}$ – Uncorrected dQ/dx in data in the collection plane

$$(dQ/dx)^{MC}_{XYZ\_Corrected} = (dQ/dx)_{Reconstructed} \cdot Corr(y,z) \cdot Corr(x) \tag{9}$$

$(dQ/dx)^{MC}_{XYZ\_Corrected}$ – Corrected dQ/dx for YZ plane and drift direction irregularities in Monte Carlo in the collection plane

$(dQ/dx)_{Reconstructed}$ – Uncorrected dQ/dx in Monte Carlo in the collection plane

5.4 dE/dx calibration of the detector

Once the dQ/dx calibration of the detector is done, we can move to get the correct particle energies. The following set of points explains the procedure we adopted to do the dE/dx calibration both in Monte Carlo and data, which is the same method described in document [30] except using stopping muons coming from the beam.

- Isolate the muon tracks coming from neutrino interactions which satisfy the cuts explained in the section 3.2 for the desired plane.
- The last 200 cm residual ranges of tracks are segmented into 5 cm wide bins, which leads to a total of 40 residual range bins : Here we select tracks which have a minimum track length of 150 cm.
- We loop over all the 3D points of selected tracks and fill out the residual range bins with dE/dx values derived using the Equation 2 by setting the the calibration constant C to a particular value : Only the 3D points that are inside the detector boundaries specified in the section 5.1 are considered here as well. Moreover here we consider only the 3D points which have a track pitch value in between 0.3 cm to 0.4 cm.
- After looping over all the tracks, we fit each of dE/dx distributions to a "Landau Convoluted Gaussian" function [26] to extract the Most Probable dE/dx Value (MPV) representing that particular residual range bin.
- We plot the MPV dE/dx values against kinetic energy of the particle : For each residual range bin, we take the middle bin value as the representative residual range value of that bin and transform that to kinetic energy using a cubic spline for the tabulated data set in the Table 1. Here this reference dataset is representing the expected kinetic energy vs. residual range profile for stopping muons in liquid argon.
- We compare the the curve generated in the previous step with the prediction made by the "Landau-Vavilov" function [31] in the MIP region of the muons (250 MeV - 450 MeV) and χ^2 value is calculated using the Equation 10. The Landau-Vavilov function describes the energy loss probability distribution for a particle in a given medium. One of the striking features of this distribution is that the most probable energy loss of a particle is dependent on the thickness of the energy absorber. So here to get the predicted MPV dE/dx, we set the absorber thickness to be 0.35 cm.
- We iterate through the the same set of steps described above several times to generate tabulated set of data between a given calibration constant (C) and χ^2 value.

Residual range (cm)	Kinetic energy (MeV)
10	0.70437
14	1.27937
20	2.37894
30	4.72636
40	7.5788
80	22.0917
100	30.4441
140	48.2235
200	76.1461
300	123.567
400	170.845
800	353.438
1000	441.476

Table 1: Tabulated values of CSDA Residual range vs. Kinetic energy for stopping muons in liquid argon [32].

- In the final step we plot the χ^2 values thus generated against calibration constants and fit that distribution with some polynomial (mostly second order) to get the calibration constant which corresponds to the lowest χ^2 value. This method is known as the "Chi Squared Minimization [30]" method.
- With the newly derived calibration constant (C), we calculate the dE/dx values using Equation 2 using calibrated dQ/dx values as the input.

After the dE/dx calibration, we compare the newly derived dE/dx values with uncorrected dE/dx values to see the effects of the new improvements (See section 6).

$$\chi^2 = \Sigma(\frac{(MPV(dE/dx)_{prediction} - MPV(dE/dx)_{Measured})^2}{\sigma^2}) \tag{10}$$

Here we sum all the data points in the kinetic energy region of 250 MeV to 450 MeV.

For Monte Carlo,

$$\sigma^2 = \delta^2_{fit}, \tag{11}$$

where δ_{fit} is the uncertainty associated with the MPV dE/dx extracted by fitting a Landau convoluted Gaussian function [26] to the energy distribution.

For data,

$$\sigma^2 = \delta^2_{fit} + \delta^2_{recombination}, \tag{12}$$

where $\delta_{recombination}$ is the systematic error associated with recombination model uncertainties (Here we take the uncertainty to be 1.5% of the measured dE/dx.

Note the Monte Carlo sample was simulated and reconstructed with the same recombination model. Therefore there is no systematic uncertainty associated with recombination model for Monte Carlo.

See note [30] for a detailed description of the above uncertainties.

6 Results

6.1 dQ/dx calibration

6.1.1 dQ/dx calibration (Monte Carlo)

The dQ/dx calibration of the detector in Monte Carlo is done using a single large dataset described in section 4. Figure 8 shows the variation of YZ and drift direction correction factors in the collection plane. Figure 9 shows the calibrated dQ/dx vs residual range for true stopping muons and stopping protons.

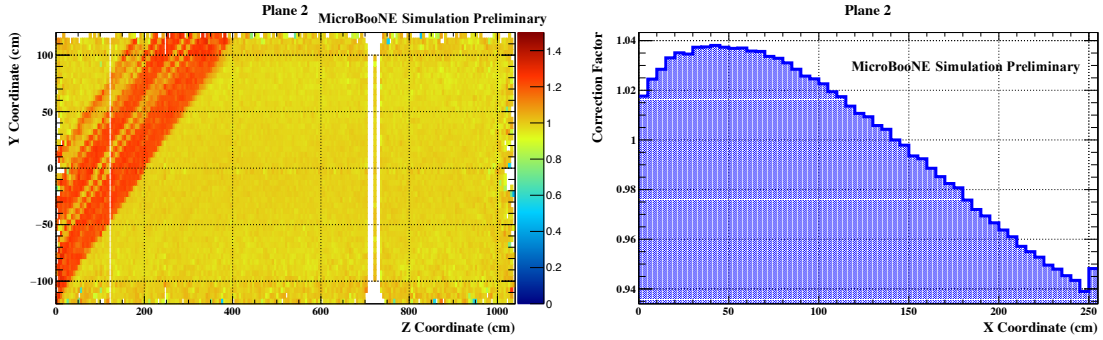

Figure 8: (Left) YZ correction factors in the collection plane in Monte Carlo. Here Z axis represents correction factors for a given 5 cm × 5 cm cell in the YZ plane. (Right) Drift direction correction factors in the collection plane in Monte Carlo.

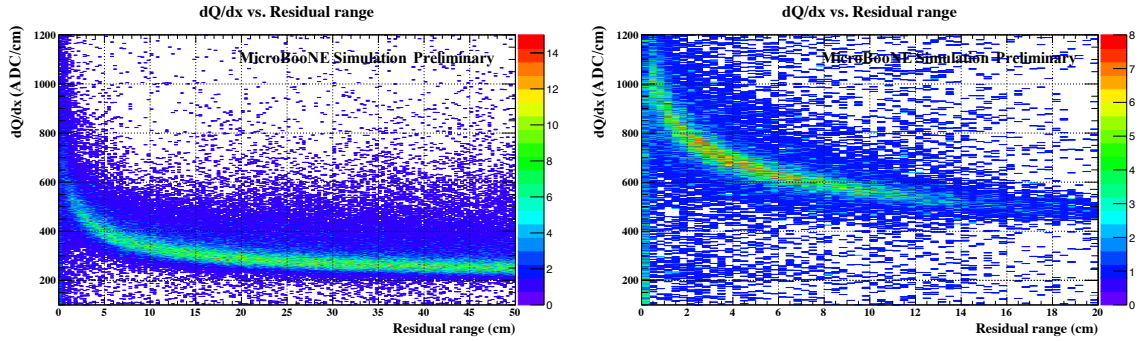

Figure 9: Calibrated dQ/dx vs residual range for true stopping muons (left) and stopping protons (right).

6.1.2 dQ/dx calibration (data)

YZ correction factors are derived for 3 separate data sets. In the first dataset, we have data combined between February and May; in the second one data from June and July are combined; and in the last dataset data between August and October are combined. See Figure 10 for the variation of YZ correction factors in the collection plane for the first dataset. As there is no significant difference between YZ correction factors derived in 3 samples, only the results for the first dataset is shown here.

The drift direction corrections factors and time corrections are derived for the time period starting from 02/10/2016 to 10/19/2016 on a daily basis. But due to lack of statistics, we are skipping some

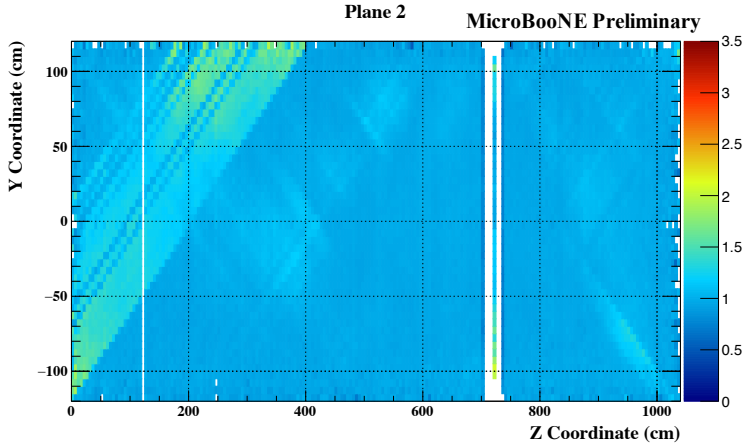

Figure 10: The variation of YZ correction factors in the collection plane for the combined time period from February to May in 2016 in data. The Z axis represents correction factors for a given 5 cm × 5 cm cell in the YZ plane.

days. See Figure 11 for the variation of time correction over time. Figure 12 shows the effect of dQ/dx calibration both in Monte Carlo and data. To create these comparison plots anode-cathode crossing cosmic muons are used.

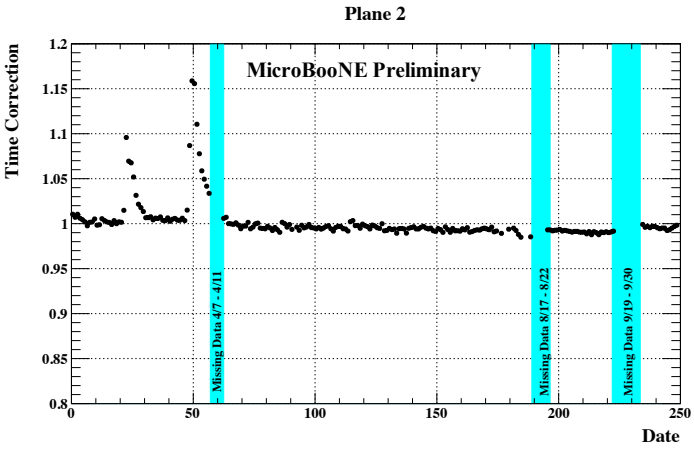

Figure 11: The variation of the time correction $C(t)$ over time in the collection plane.

6.2 dE/dx calibration

The absolute calibration of the detector is done using both Monte Carlo and data. Figure 13 shows $\chi^2 - \chi^2_{Min}$ vs Calibration Constant C for the collection plane. The best fit value is the one that gives the minimal χ^2. The uncertainty is determined by $\Delta\chi^2 = \chi^2 - \chi^2_{Min} = 1$

The calibration constants derived for the collection plane are shown in Table 2. The Monte Carlo calibration constant uncertainty is statistical only. The data calibration constant uncertainty include both the statistical uncertainty and the recombination uncertainty. Figure 14 shows the comparison between prediction and the measured MPV dE/dx with these calibration constants for stopping muons both in Monte Carlo and data.

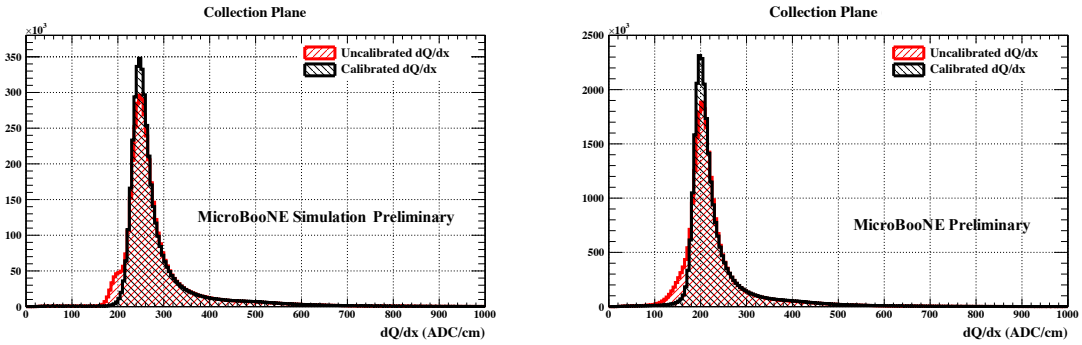

Figure 12: (Left) Comparison of calibrated and uncalibrated dQ/dx in Monte Carlo using crossing muons in the collection plane. (Right) Comparison of calibrated and uncalibrated dQ/dx in data using crossing muons in the collection plane.

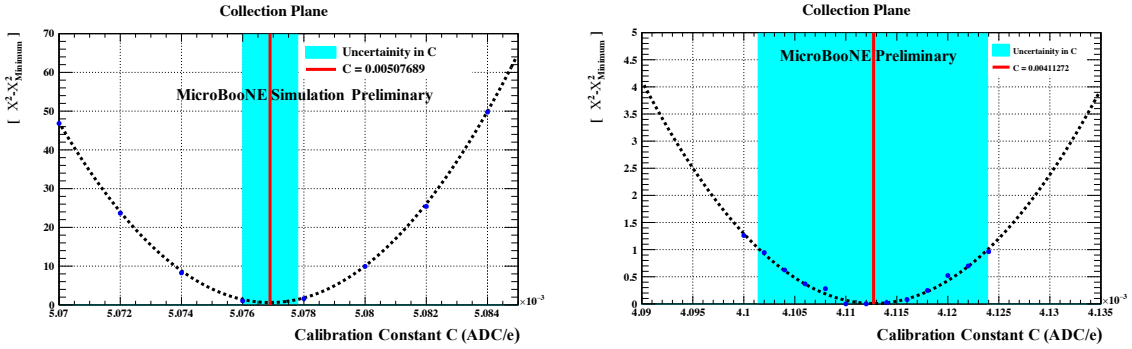

Figure 13: Distributions of $\chi^2 - \chi^2_{Min}$ vs Calibration Constant C for the collection plane. The color bands show the uncertainty associated with calibration constant C. The units of the X-axis is ADC per electron. (Left) Monte Carlo. (Right) Data.

Table 2: Calibration constants and $\chi^2_{Min}/d.o.f$ for the collection plane in Monte Carlo and data. The units of the calibration constants are ADC per electron.

	Monte Carlo (ADC/e)	Data (ADC/e)
Calibration Constant	$(5.076 \pm 0.001) \times 10^{-3}$	$(4.113 \pm 0.011) \times 10^{-3}$
$\chi^2_{Min}/d.o.f$	$15.0/18 \sim 0.84$	$5.12/18 \sim 0.28$

Figure 15 shows the calibrated dE/dx vs residual range for the Monte Carlo true stopping muons and protons. The measured dE/dx profiles agree very well with the expectations.

6.2.1 Validation of calorimetric energy reconstruction

The absolute energy-scale calibration can be validated in a data-driven way by comparing the range-based energy to that obtained via calorimetry for selected stopping muon candidates in data. For each selected stopping muon track, the range vs. calorimetric kinetic energy are computed, and the fractional difference between these methods is shown in figure 16. The agreement between the two, of order 3%, gives confidence in the proper absolute energy-scale calibration to within this level

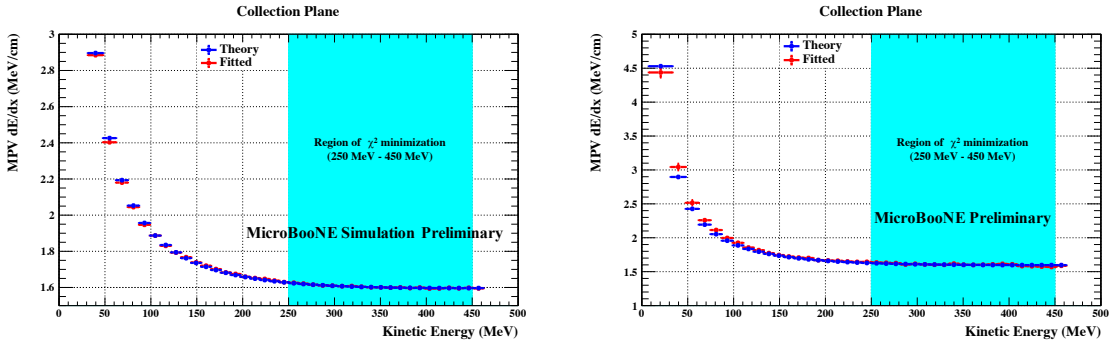

Figure 14: ((Left) Comparison between the prediction and the fitted MPV dE/dx for stopping muons in Monte Carlo in the collection plane. (Right) Comparison between the prediction and the fitted MPV dE/dx for stopping muons in data in the collection plane.

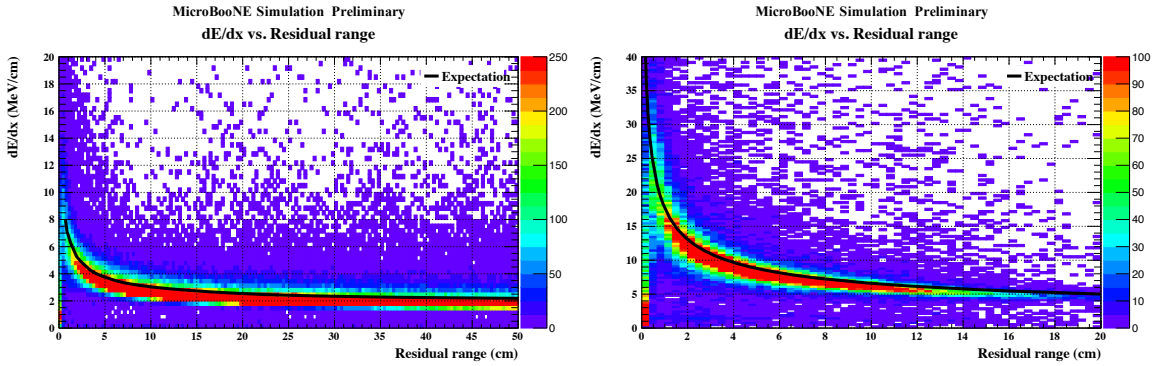

Figure 15: Calibrated dE/dx vs residual range for true stopping muons (left) and protons (right). The overlaid curves are expected mean dE/dx vs. residual range.

of agreement, and provides a closure test for this calibration.

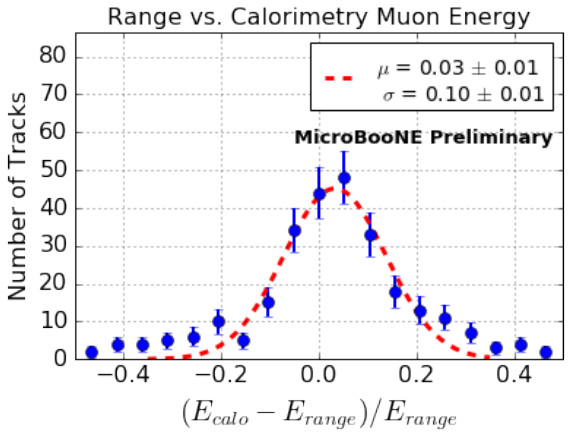

Figure 16: Fractional difference in range vs. calorimetric kinetic energy for selected stopping muons in data. The distribution is fit to a Gaussian which returns a mean of 0.03 and width of 0.10.

7 Angular dependence study

The calibration procedure described in the public note does not make any angular dependent corrections. The angular distributions of the anode-cathode crossing muons are shown in Figure 6. In order to study the angular dependence of the dQ/dx (relative) calibration, we divide the crossing muons into 4 angular bins:

- $0° < |\theta_{xz}| < 50°$
- $50° < |\theta_{xz}| < 75°$
- $105° < |\theta_{xz}| < 130°$
- $130° < |\theta_{xz}| < 180°$

and derive the YZ and X correction factors for each subsample following the same procedure described above. All the other selection criteria remain the same.

Figure 17 shows the percentage differences in YZ correction factors in all YZ cells between different subsamples and all samples combined for the collection plane. The shift of the mean of the distribution away from zero is indicative of the amount of bias observed in a given angular bin. There are more data tracks than MC tracks so the data distributions are narrower. The peaks of the four distributions all agree within 1%, which indicates the angular dependence of the YZ correction is small for collection plane.

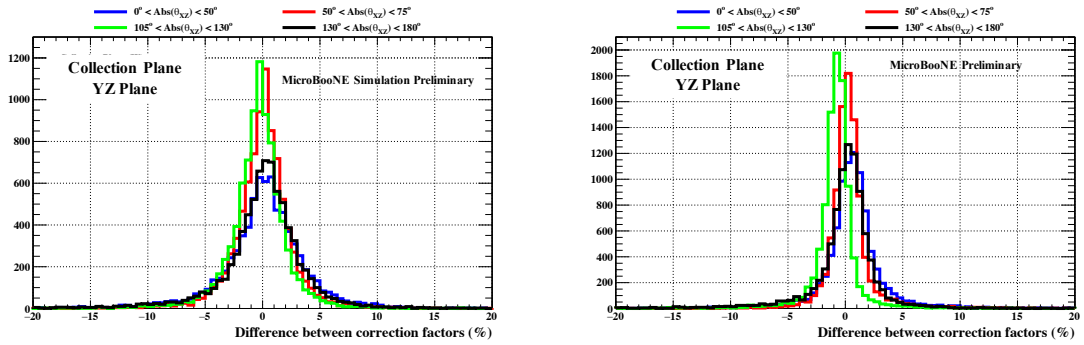

(a) Collection plane, MC

(b) Collection plane, data

Figure 17: Percentage differences in YZ correction factors in all YZ cells between different subsamples and all samples combined.

Figure 18 shows the percentage differences in X correction factors between different subsamples and all samples combined for the collection plane. The collection plane shows very small angular dependence.

Based on the above studies, we assign 1% systematic error on the YZ correction and 1.5% systematic error on the X correction for the collection plane.

8 Conclusions

In this public note, we describe for the first time a method that calibrates a LArTPC using cosmic ray muons. We use through-going muons to remove spatial and temporal variations in the detector response. We use stopping muons to determine the absolute energy scale. The calibrated energy loss agrees very well with the expectation, which helps with the particle identification and energy reconstruction. This method can be used by other LArTPC experiments to calibrate their detectors. Here are a few observations we would like to highlight.

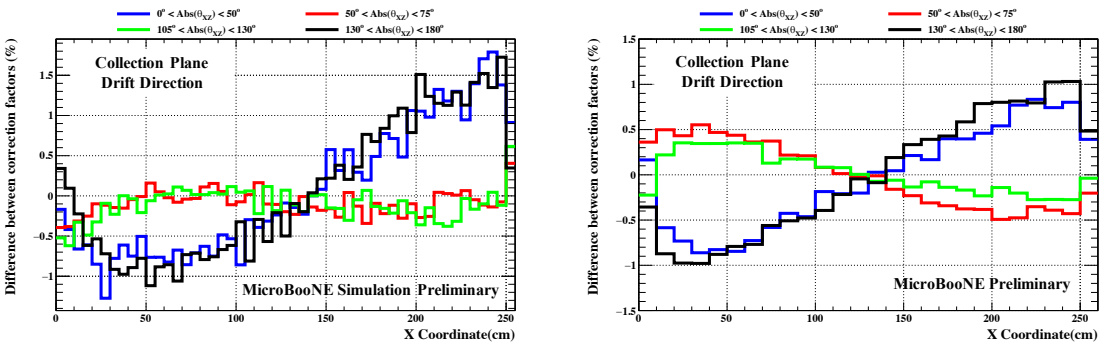

(a) Collection plane, MC

(b) Collection plane, data

Figure 18: Percentage differences in X correction factors between different subsamples and all samples combined.

- By looking at the YZ correction factors derived for data and Monte Carlo, the dQ/dx response seems uniform in the collection plane. See Figures 8 (Left) and 10. Moreover we can see the same features in these plots, indicating the simulations of the collection plane are in agreement with data.
- The drift direction correction factors and time corrections are very uniform in time in the collection plane except for a few low purity datasets. See Figure 11. There is a slight increase of detector response over time (Figure 7), which is being investigated.
- The effectiveness of the dQ/dx calibration is shown in Figure 12. Here it can be seen that the current dQ/dx calibration makes the distributions more sharply peaked in the collection plane by minimizing the detector effects which smear out the dQ/dx spectrum.
- In Figure 14 we see a good agreement between the prediction and the measured dE/dx both in data and Monte Carlo for the given calibration constants. In data the measured dE/dx is slightly higher than theory at low kinetic energy. This is an indication of a mismodeling of the recombination effect.
- The calibration constant derived at Monte Carlo level is $(5.076 \pm 0.001) \times 10^{-3}$ ADC/e, which approximately matches with the input calibration constant of Monte Carlo 5×10^{-3} ADC/e. In data the calibration constant derived is $(4.113 \pm 0.011) \times 10^{-3}$ ADC/e. In addition, comparison between kinetic energies calculated using calorimetry after the dE/dx calibration and kinetic energies calculated using track range agree within 3%. The bias is consistent with the discrepancy in the dE/dx measurement at low kinetic energy mentioned above.
- Figure 15 shows the calibrated dE/dx profiles for stopping muons and protons which agree with the expectation. This is crucial for the successful particle identification using calorimetric information.

Acknowledgements

We would like to thank Tom Junk (FNAL) for the useful discussions on statistical analysis

References

[1] The MicroBooNE Collaboration, "Design and construction of the MicroBooNE detector", JINST 12, P02017 (2017).

[2] The MicroBooNE Collaboration, "Ionization Electron Signal Processing in Single Phase LAr TPCs I: Algorithm Description and Quantitative Evaluation with MicroBooNE Simulation", arXiv:1802.08709, submitted to JINST.

[3] The MicroBooNE Collaboration, "Ionization Electron Signal Processing in Single Phase LAr TPCs II: Data/Simulation Comparison and Performance in MicroBooNE", arXiv:1804.02583, submitted to JINST.

[4] The MicroBooNE Collaboration, "Noise Characterization and Filtering in the MicroBooNE Liquid Argon TPC", arXiv:1705.07341, JINST 12, P08003 (2017).

[5] The MicroBooNE Collaboration, "Study of space charge effects in MicroBooNE", MICROBOONE-NOTE-1018-PUB (2016).

[6] Michael Mooney, "The MicroBooNE Experiment and the impact of Space Charge Effects", arXiv:1511.01563 (2015).

[7] E. Buckley *et al.,* "A study of ionization electrons drifting over large distances in liquid argon", Nucl. Instrum. and Methods in Physics Research A 275, 364-372 (1989).

[8] A. Bettini *et al.,* "A study of the factors affecting the electron lifetime in ultra-pure liquid argon", Nucl. Instrum. and Methods in Physics Research A 305, 177-186 (1991).

[9] S. Amoruso *et al.,* "Analysis of the liquid argon purity in the ICARUS T600 TPC", Nucl. Instrum. and Methods in Physics Research A 516, 68-79 (2014).

[10] The LongBo Collaboration, "Design and operation of LongBo: a 2 m long drift liquid argon TPC", JINST 10, P07015 (2015).

[11] The MicroBooNE Collaboration, "Measurement of the Electronegative Contaminants and Drift Electron Lifetime in the MicroBooNE Experiment", MICROBOONE-NOTE-1003-PUB (2016).

[12] The MicroBooNE Collaboration, "A Measurement of the Attenuation of Drifting Electrons in the MicroBooNE LArTPC", MICROBOONE-NOTE-1026-PUB (2017).

[13] C. Anderson, et al., The ArgoNeut detector in the Numi low-energy beam at Fermilab, JINST 7, P10019 (2012).

[14] J. J. Hartnell, "Measurement of the Calorimetric Energy Scale in MINOS," FERMILAB-THESIS-2005-51, doi:10.2172/875528.

[15] The ArgoNeuT Collaboration, "A study of electron recombination using highly ionizing particles in the ArgoNeuT Liquid Argon TPC", JINST 8, P08005 (2013).

[16] M. Antonello *et al.,* "Experimental observation of an extremely high electron lifetime with the ICARUS-T600 LAr-TPC", JINST 9, P12006 (2014).

[17] A. Ereditato *et al.,* "Design and operation of ARGONTUBE: a 5 m long drift liquid argon TPC", JINST 8, P07002 (2013).

[18] A. A. Aguilar-Arevalo *et al.,* "Unexplained Excess of Electron-like Events from a 1 GeV Neutrino Beam", Phys. Rev. Lett. **102**, 101802 (2009).

[19] A. A. Aguilar-Arevalo *et al.,* "A Combined $\nu_\mu \to \nu_e$ and $\bar{\nu}_\mu \to \bar{\nu}_e$ Oscillation Analysis of the MiniBooNE Excesses", Phys. Rev. Lett. **110**, 161801 (2013).

[20] Sigma-Aldrich, P.O. Box 14508, St. Louis, MO 63178 USA.

[21] BASF Corp., 100 Park Avenue, Florham Park, NJ 07932 USA.

[22] E. D. Church, "Larsoft: A software package for liquid argon time projection drift chambers", arXiv:1311.6774 (2016).

[23] The ArgoNeuT Collaboration, "Analysis of a large sample of neutrino-induced muons with the ArgoNeuT detector", JINST 7, P10020 (2012).

[24] The MicroBooNE Collaboration, "Establishing a Pure Sample of Side-Piercing Through-Going Cosmic-Ray Muons for LArTPC Calibration in MicroBooNE", MICROBOONE-NOTE-1028-PUB (2017).

[25] MicroBooNE collaboration, "Measurement of Cosmic Ray Reconstruction Efficiencies in the MicroBooNE LAr TPC Using a Small External Cosmic Ray Counter", arXiv:1707.09903, JINST 12, P12030 (2017).

[26] Convoluted Landau and Gaussian Fitting Function, https://root.cern.ch/root/html/tutorials/fit/langaus.C.html

[27] The MicroBooNE Collaboration, "Selection and kinematic properties of numu charged-current inclusive events in 5E19 POT of MicroBooNE data", MICROBOONE-NOTE-1010-PUB (2016).

[28] D. Heck, G. Schatz, T. Thouw, J. Knapp and J. N. Capdevielle, FZKA-6019.

[29] MicroBooNE collaboration, "The Pandora Multi-Algorithm Approach to Automated Pattern Recognition of Cosmic Ray Muon and Neutrino Events in the MicroBooNE Detector", arXiv:1708.03135, Eur. Phys. J. C78, 1, 82 (2018).

[30] The MicroBooNE Collaboration, "Calibration of the MicroBooNE TPC's Energy Response with Cosmic-Ray Stopping Muons", TECH NOTE-9149-v5.

[31] Passage of particle through matter, http://pdg.ge.infn.it/2014/reviews/rpp2014-rev-passage-particles-matter.pdf

[32] Donald E. Groom, Nikolai V. Mokhov, Sergei I. Striganov, Muon Stopping Power and Range Tables 10 MeV - 100 TeV, Atomic Data and Nuclear Data Tables, Vol. 76, No. 2, July 2001.

[33] The DUNE 35-ton Prototype Collaboration, "Evidence of Impurity Stratification in the DUNE 35 ton Prototype Cryostat", FERMILAB-TM-2642-ND (2017).

[34] The ICARUS Collaboration, "Measurement of the μ decay spectrum with the ICARUS liquid Argon TPC", Eur. Phys. J. C 33, 233 (2004).

[35] A. Ereditato *et al.,* "A steerable UV laser system for the calibration of liquid argon time projection chambers", JINST 9, T11007 (2014).

Appendix A

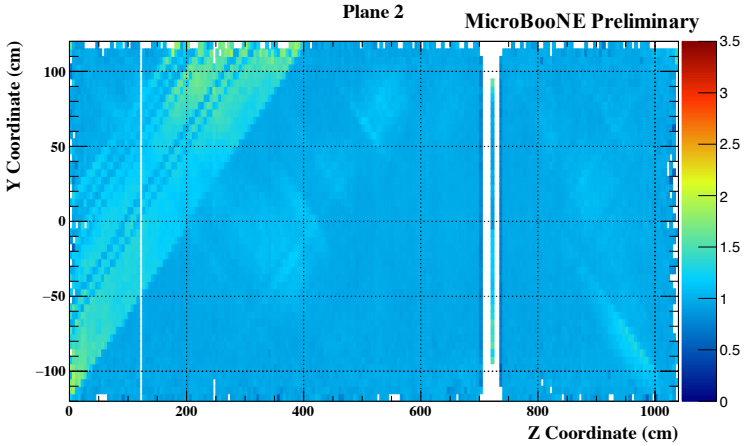

Figure 19: The variation of YZ correction factors in the collection plane for the combined time period of June and July in data. The Z axis represents correction factors for a given 5 cm × 5 cm cell in the YZ plane.

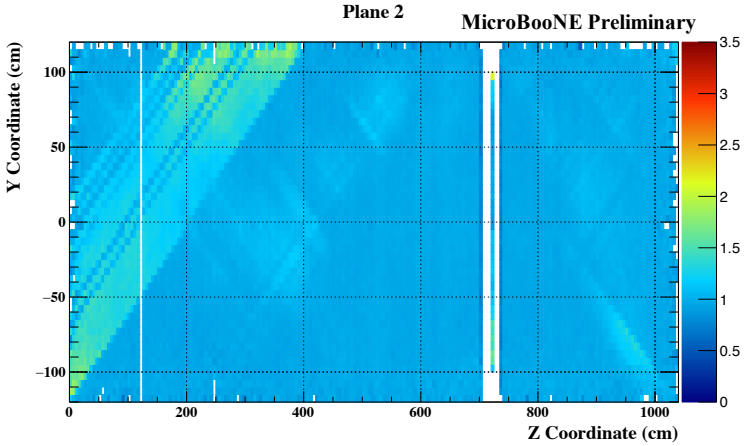

Figure 20: The variation of YZ correction factors in the collection plane for the combined time period of months August, September and October in data. The Z axis represents correction factors for a given 5 cm × 5 cm cell in the YZ plane.